SIDESLIP AERODYNAMICS FOR HYTEX SPACE VEHICLE

Mattias Sillén

Saab Military Aircraft
S-581 88 Linköping, Sweden

Abstract

The objectives of the German Hypersonics Technology Programme were to develop the major enabling technologies for a future advanced space transportation system, based on aerodynamic flight and airbreathing propulsion. Aerodynamic investigations performed on an early design of the SÄNGER concept revealed large discrepancies in the lateral aerodynamic coefficients between windtunnel results and inviscid computations for sideslip cases. Viscous effects were suspected to be the origin of these discrepancies.
In the present paper the influence of viscous effects on the aerodynamics of a hypersonic vehicle in sideslipe is investigated. This is accomplished by computationally obtaining the flowfields governed by viscous and inviscid flow. The configuration chosen is a demonstrator concept studied in the German Hypersonics Technology Programme, designated Hytex R-A_3. The flight case is defined by a Mach number of 3.5 at altitude 17.5 km, an angle of attack of 2.01^o and a sideslip angle of -5.0^o. Computational grids are generated for the viscous and inviscid computations containing 2.30 and 1.05 million points respectively.
The two flowfields behave very similarly near the forebody but show topological differences further downstream on the vehicle. This also applies to the surface pressure distribution. However, when examining the integrated forces and moments only smaller differences are seen, except for a somewhat larger difference in yawing moment and a 40% increase of the drag in the viscous solution due to the friction drag.

Introduction

With the launch of Sputnik in 1957 the space became accessible to man. Since then the advancements in technology has led to major improvements in all fields of transportation with one exception, space transportations. Most of the payloads today are launched with the same type of expendable launchers used decades ago. Several studies have concluded that the present space launch systems are expensive and labour intensive and have to be replaced in the future by more cost-efficient systems.

Numerous programmes in Europe as well as in the United States, Russia and Japan have studied the possibility to develop a reusable space launch system. Examples are the US NASP and X-33-projects, the Japanese Space Plane-project and the German SÄNGER project[10].

The work performed so far in the different programmes has given many important results. It has also revealed a number of critical technology areas that must be adressed before a cost-efficient safe space transportation system with low environmental impact can become reality. Among the key technology areas[5] that need concentrated development are propulsion, aerothermodynamics, materials and structure as well as guidance and control.

For an airbreathing hypersonic vehicle a very strong coupling of propulsion, aerothermodynamics, materials and structure, and flight dynamics exist, which must be taken into account in the design of the vehicle. Problematic issues are for example the airframe/propulsion integration, the efficiency of the inlet over a large Mach number range and the heat loads. A designer facing these and other design problems must be supported both by design tools and simulation tools. In aerothermodynamics two major classes of simulation means are available: computational simulation and experimental simulation.
Both classes of simulation have their benefits and disadvantages. Experimental simulation uses sub-scale models which leads to large simulation-parameter deficiencies. In computational simulation flow-physics (turbulence, transition) and thermodynamics (surface catalytic processes etc.) pose large modelling problems. Both methods of simulation are used and must be used to complement each other in the design process.

Within the German Hypersonics Technology Programme a hypersonic demonstrator called Hytex R-A_3 was designed. With a ramjet/scramjet propulsion system it is aimed for Mach numbers up to 6.8.
The present paper investigates the aerodynamic behavior in sideslip for the Hytex R-A_3 vehicle. The reason for this is that during the evaluation of the stability and control data for an earlier design, called SÄNGER 8-88, results from wind tunnel tests and inviscid numerical simulations revealed large discrepancies in sideslip aerodynamics. It was

assumed that viscous effects might play a major role in these problems. To thoroughly examine the difference between viscous and inviscid flow, large scale viscous and inviscid calculations are performed around the Hytex R-A_3 configuration.

The following sections describe the physical modelling and the numerical implementation used in the simulations. The generation of the computational grids for the viscous and inviscid simulations is described and a thorough evaluation of the flow is given for this complex geometry with emphasis on sideslip behavior.

Numerical Flow Simulation

The use of Computational Fluid Dynamics (CFD) analysis as an integrated part of the design process requires a robust, efficient and well validated system. This includes everything from the grid generation over the flow solver to the postprocessing tools. The 3D Navier-Stokes code Multnas is developed at Saab to efficiently compute stationary compressible viscous and inviscid flow around complex configurations. Considerable effort is spent turning Multnas into a general solver for various CFD applications in the aerospace field. The ability to successfully compute complex supersonic/hypersonic flow has been developed through participation in various international hypersonic technology projects, as the ESA Hermes project[9] and the German Hypersonics Technology Programme[4].

Numerical Scheme

Multnas uses structured multiblock grids where each block surface can be subdivided into patches where different boundary conditions can be applied. The discretization is a cell centred finite volume formulation made popular by Jameson[6].

Let ρ be the density, u, v and w the velocity components in the three coordinate directions and E the total internal energy. The solution vector is then

$$U = (\rho, \rho u, \rho v, \rho w, \rho E)^T \tag{1}$$

For the generally written Navier-Stokes equations

$$\frac{\partial U}{\partial t} + \nabla H = 0 \tag{2}$$

with the tensor H incorporating the convective and viscous terms, the finite volume formulation for a cell with the volume W can be expressed as

$$\frac{\partial U}{\partial t} W + C(U) - V(U) - D(U) = 0 \tag{3}$$

Here $C(U)$ and $V(U)$ denote the summation of convective and viscous fluxes, respectively, over the surfaces of the cell, and $D(U)$ is the artificial dissipative term. The artificial dissipation is of scalar anisotropic type, where the blend of second and fourth order terms is guided by a three point stencil pressure sensor.

The integration in time of the discretized partial differential equations is performed with an iterative solver. Let U be the solution vector for all cells in the grid and let r(U) denote the residual of the spatial discretization of the Navier-Stokes equations. To solve the system of equations

$$r(U) = 0 \tag{4}$$

an explicit Runge-Kutta scheme is applied. The algorithm for a k-stage Runge-Kutta scheme is

$$\begin{aligned} U^0 &= U^{n-1} \\ U^i &= U^0 + \alpha_i \Delta t r(U^{i-1}), \; i = 1, \ldots, k \\ U^n &= U^k \end{aligned} \tag{5}$$

for the *nth* iterative step. The constants α_i are chosen to be

$$(\alpha_1, \alpha_2, \alpha_3, \alpha_4, \alpha_5) = (0.25, 0.167, 0.375, 0.5, 1.0) \tag{6}$$

for a five stage algorithm. Local time steps as well as multigrid technique are available for convergence acceleration. The multigrid technique is based on a Full Approximation Scheme (FAS).

Turbulence Modelling

The Navier-Stokes equations model the flow of air around aeroplanes very well. A difficulty is that turbulent flow has many different scales in space and time. In the numerical solution of Navier-Stokes equations these scales cannot be resolved, except for low Reynolds numbers and simple geometries, with present day computers, due to insufficient memory capacity and cpu speed. The influence of turbulence must therefore be modelled. A commonly used approximation level is the two-equation turbulence models. Two additional transport equations are solved to model the turbulent contribution to the viscous flow.

Multnas is equipped with a low Reynolds number two-equation turbulence model of κ-ε type according to Launder-Sharma[7].

Applying the Boussinesq eddy viscosity concept to the Favre averaged Navier-Stokes equations relates the Reynolds stresses to the mean flow variables and yields a way to close the system.

$$-\overline{\rho u''_i u''_j} = \mu_T S_{ij} - \frac{2}{3}\bar{\rho}\kappa\delta_{ij} \tag{7}$$

where u''_i is the fluctuating part of the velocity variables, μ_T is the eddy viscosity, S_{ij} is the strain rate tensor and κ is the turbulent kinetic energy.

The eddy viscosity is obtained from

$$\mu_T = C_\mu f_\mu \rho \frac{\kappa^2}{\varepsilon} \tag{8}$$

where ε is the turbulent dissipation rate and C_μ and f_μ are model constants.

The turbulent kinetic energy and its dissipation rate are determined from the steady state transport equations stated below:

$$(\rho u_k \kappa)_{,k} = -\rho D + \left(\mu_T S_{ij} - \frac{2}{3}\rho\kappa\delta_{ij}\right)u_{i,j} - \rho\varepsilon\left(1+\alpha_1 M_T^2\right) + \left[\left(\mu + \frac{\mu_T}{\sigma_k}\right)\kappa_{,j}\right]_{,j} \quad (9)$$

$$(\rho u_k \varepsilon)_{,k} = \rho E + C_{\varepsilon 1} f_1 \frac{\varepsilon}{\kappa}\left(\mu_T S_{ij} - \frac{2}{3}\rho\kappa\delta_{ij}\right)u_{i,j} - C_{\varepsilon 2} f_2 \rho\frac{\varepsilon^2}{\kappa} + \left[\left(\mu + \frac{\mu_T}{\sigma_\varepsilon}\right)\varepsilon_{,k}\right]_{,k} \quad (10)$$

$$\rho D = 2\mu|\nabla\sqrt{\kappa}|^2 \quad (11)$$

$$\rho E = \frac{2\mu\mu_T}{\rho}(\nabla^2 U)^2 \quad (12)$$

where $C_{\varepsilon 1}$ is a constant and $C_{\varepsilon 2}$, f_1 and f_2 are wall damping functions to properly model the near wall behavior. In this implementation, however, $C_{\varepsilon 2}$ will be treated as a constant. The additional source terms ρD and ρE are model specific terms to better represent the near wall behavior.

$$f_\mu = exp\left(-\frac{3.4}{(1+R_T/50)^2}\right) \quad (13)$$

$$f_2 = 1 - 0.3exp\left(-R_T^2\right) \quad (14)$$

$R_T=\rho\kappa^2/(\mu\varepsilon)$ is the turbulent Reynolds number.
To account for compressibility effects observations by Sarkar et.al.[8] are used with α_1 equal to unity and the turbulent Mach number $M_T^2 = \kappa/c^2$, where c is the speed of sound. A major advantage of this model is that it does not contain any explicit dependence on the distance from the walls, which can be complicated to obtain for very general geometries.

The constants used in the model are:

$$\begin{aligned} C_\mu &= 0.09 \\ C_{\varepsilon 1} &= 1.44 \\ C_{\varepsilon 2} &= 1.92 \\ \sigma_k &= 1.0 \\ \sigma_\varepsilon &= 1.3 \end{aligned} \quad (15)$$

The numerical implementation is implicit, solving the steady transport equations by ADI technique[3]. One relaxation sweep is performed in each direction after every complete Runge-Kutta cycle for the flow equations. The spatial derivatives are evaluated using finite volume technique, with hybrid central/upwind differencing.

Boundary Conditions

The flow around the HYTEX vehicle is highly influenced by the engine and the inlet/exhaust, see Figure 1. To reasonably well simulate the flow around the complete vehicle a model of the engine must be provided. This is accomplished by introducing the engine exhaust as a boundary condition. The outflow from the engine is fully known with density, velocity components in the three space directions and pressure. The flow is supersonic at the engine exit and hence all local characteristics are pointing into the external flow field. All variables are therefore given at the engine exhaust boundary, giving a simple model of the engine.
Calculations are performed inside the ramp section of the inlet and ends with an extrapolated supersonic boundary condition downstream of the intake duct's entry.
At the external inflow/outflow boundary Riemann invariants are applied.

Low Pressure Flow

Solving the Euler equations around objects with base area in the higher velocity range, i.e. supersonic or hypersonic flow, can be troublesome. In the separated low pressure region behind the base often negative pressure values show up. This occurs in the present case in regions behind the thick trailing edges of the main wings and the fin. As negative pressure regions are unphysical phenomena disturbing the numerical solution of the flow, a way around the problem is found. By requiring the internal energy to always remain positive, negative pressure regions are avoided. This problem does not appear in the viscous solution due to the more complete description of the flow given by the Navier-Stokes equations.

Geometry and Grid Generation

An overview of the HYTEX R-A_3 geometry is given in Figure 1. The winged vehicle is approx. 15.4 m in length with a semi-span of 1.9 m. At the lower rear section the propulsion system is located. The first compression ramp is fixed and the second is deflectable to provide a shock on lip situation for all flight cases.
Two calculations are performed, one viscous and one inviscid. The computational grids for these cases differ at one major point, the near wall treatment. In the grid for the viscous computation the boundary layer close to the surface must be well resolved to obtain an adequate solution. The grid outside the boundary layer and the surface grid are practically the same in the two cases. This gives the inviscid grid a total of 1.05 million points and the grid for the viscous calculation adds up to 2.30 million points for a full sideslip model. On the surface approx. 41 000 points are distributed. A y^+ value of about 1-2 is chosen for the first point above the surface to minimize the size of the grid and yet provide a decent resolution of the boundary layer in the viscous grid. In the normal direction the stretching function of Blottner[1] is applied. The thickness of the first cell, ds_1, is selected and the other satisfy:

$$ds_j = ds_{j-1}\left(1 + \varepsilon\sin\frac{\pi(j+1)}{2(N+1)}\right) \quad (16)$$

with ε chosen large enough for the points to reach the outer boundary. N is the number of points in the direction normal to the surface.

Building a structured multiblock grid around a complex vehicle like the HYTEX R-A_3 is not a straight forward task. It gets even more complicated when computing a sideslip case, with the doubling in required number of points, and at the same time having an upper number of points limit on what is acceptable with the available computers. The chosen block topology is aimed at reducing the number of points needed in the grid. Around the body, the wings, the tail-plane and the fin separate thin blocks are generated with O-topology to resolve the leading and trailing edges as well as the tips. Within these blocks most of the boundary layer in the flow is situated. They can be seen as a shell outside the vehicle surface, see Figure 2. These shell type blocks are connected to each other and the outer boundary by a number of other blocks. In this way the number of points are kept to a minimum, not allowing dense point distributions in the boundary layer to propagate to the outer boundary. The surface grid is given in Figure 3 and cross plane grid surfaces at the nose and at the main wings for the Navier-Stokes grid are seen in Figure 4. Only the port side is plotted in Figure 2 and Figure 3.

The grid is extended into the compression ramp region in the engine inlet. Downstream of the intake duct's entry the grid ends with a supersonic outflow boundary. The surface grid is generated in patches that facilitates the removing of surfaces in the engine inlet and expansion ramp regions when evaluating the aerodynamic forces and moments of the vehicle.

Numerical Solution of Viscous and Inviscid Flow Fields

The specific flight case that is studied here is described by a free stream Mach number of 3.5, and an angle of attack of 2.01° at 17.5 km altitude. The sideslip angle is -5.0°. In this case the flow over the vehicle is assumed to be fully turbulent with a Reynolds number of 9.5 millions per meter. The free stream temperature is 216 K and at the vehicle surface a constant temperature of 580 K is prescribed, which corresponds to a radiation-adiabatic surface with an emissivity factor of 0.85.

At the engine exhaust boundary are the following values used:

$$T_0 = 2483K$$
$$p_0 = 259.5kPa \qquad (17)$$
$$M = 2.81$$

The exit velocity is fully aligned with the boundary normal. The flow is assumed to be a calorically perfect gas, which gives good accuracy for air temperatures below 1000 K. The exhaust gas from the engine has higher temperature and a different composition but is however for simplicity regarded as a perfect gas with the same gas constant and γ as the rest of the flow field. This is not a substantial source of error as the major interest of this investigation is in the comparison between viscous and inviscid solutions of the flow field. The computational grids are not adapted to fully resolve the flow behavior near the engine exit with shocks and slip surfaces.

The computations are initiated on a coarse grid with free stream conditions. The turbulent variables are initially set to very low values, 10^{-10}, resulting in negligible free stream turbulence. The coarse grid solution is interpolated onto the fine grid to serve as a start solution. The fine grid solution is iterated until the aerodynamic coefficients are stabilized. A reduction of the rms residual based on the density of approx. 3 orders of magnitude is reached in both the viscous and the inviscid calculation.

Computational Results

The flow around the HYTEX vehicle in sideslip at supersonic speed is complex. The outer flow regions are dominated by a bow shock, a shock in front of the engine intake, the wing leading edge shocks and a crossflow shock at the fin. The shock patterns for the two solutions are quite similar, except for a crossflow shock on the leeside wing in the inviscid solution, see Figure 5, where the intake and leading edge shocks are seen at a cross section at the main wings. The shock patterns are visualized as the divergence of the velocity. The strength of the shocks is weaker in the viscous solution due to the smoothing effect of the viscosity.

Examining the flow closer to the vehicle surface reveals larger differences in flow behavior between the viscous and inviscid solutions. Comparing the skin friction lines in the viscous solution with surface velocity streamlines in the inviscid solution exposes both similarities and differences in the near surface flow. The viscous skin friction lines are plotted in Figure 6, indicating separation and reattachment lines. The corresponding streamlines near the vehicle surface in the inviscid case are depicted in Figure 7. The flow in the nose region is quite similar for the two solutions. Close to the nose the flow on the leeward body side is attached but further downstream a separation occurs in both solutions. From the wingstation and downstream the flow in the viscous solution shows a much more complex pattern compared to the inviscid solution, with several separated regions and vortices.

The skin friction lines in the viscous solution indicate a number of separated regions. This can also be seen in the total pressure cross section plot in Figure 8. A large cross flow separation occurs at the upper side of the body, from the wing position and downstream. The reattachment takes place further down on the leeside body side. Having the same reattachment line but rotating in opposite direction is a vortex separating at the leeside wing, see also Figure 9 where velocity vectors are plotted in a cross section at the leeside wing. At the leeward side of the propulsion system wall the flow separates, and creates a vortex below the leeside wing. Downstream of the wing these two vortices mix and create a complex flow pattern. At the tail-plane coun-

terclockwise rotating vortices are formed on both sides. In Figure 10 velocity vectors are plotted at a section across the fin together with skin friction lines. The separation on the windward side occurs at the body/tail-plane junction with reattachment close to the fin. For the vortex on the leeside the separation occurs near the root of the fin and the reattachment takes place at the leeside tail-plane. On the windward side only minor vortices are formed near the body/wing junction.

The inviscid solution does not exhibit the same amount of complex flow phenomena but is characterized by two major events on the leeside: the separation surface on the leeside of the body and the large vortex below the leeside wing, generated by a separation at the propulsion system leeside wall.

Examining the surface pressure of the two solutions in more detail does not reveal any dramatic differences. They are very similar at the front part of the vehicle and exhibit small differences from the wing section and downstream. The pressure coefficient for the two solutions are plotted at two different cross sections along the body in Figure 11 and Figure 12. The arrows are pointing out of the surface in case of suction. The length of the arrows indicate the absolute value, which also is indicated by a connecting curve along the arrows. At the first cross plane in the nose region there are no visible differences in surface pressure distribution. The second cross plane surface pressure distributions, through the main wings, show more marked differences. The difference is most obvious on the leeside and at the upper part of the body. This is also where the flow topology differs most between the viscous and inviscid solutions, with larger separated areas in the viscous solution. There are however differences also on the windward side, looking at Figure 13, where the pressure distribution is plotted along the wing chord for a section on both wings. The chord section, close to the wing/body junction, shows differences in pressure on both windward and leeward side. Further out towards the wingtips the two solutions give almost identical surface pressure distribution along the chord.

The differences seen in the plotted pressure distributions along the vehicle are however not completely reflected in the integrated forces, cf. Table 2 . They are evaluated according to a bookkeeping method where the contribution from surfaces in the inlet and at the expansion ramp are excluded. The corresponding values from the HYTEX R-A_3 6 degrees of freedom aerodynamic data set[(2)] are given for comparison. These data are mainly based on approximate methods and linear potential methods but some Euler calculations are performed for the sideslip aerodynamics. The reference data for the HYTEX R-A_3 vehicle is given in Table 1 .

Table 1 Reference data for HYTEX R-A_3

Ref data	
x_{ref}	11.12 m
y_{ref}	0.0 m
z_{ref}	1.8 m
S_{ref}	20.0 m^2
c	15.42 m
b	1.95m

Table 2 Aerodynamic coefficients integrated from viscous and inviscid flow solutions

Aerod. coeff.	Navier-Stokes	Euler	HYTEX Aero data
C_C	-0.0500	-0.0498	-0.053
C_l	0.0084	0.0083	0.008
C_m	-0.0004	0.0001	-0.0012
C_n	-0.0249	-0.0237	-0.026
C_L	0.0259	0.0258	0.025
C_D	0.0139	0.0101	0.014

The differences between the present Euler and Navier-Stokes results, as seen in Table 2 above, are very small. The largest effect is obtained in the drag, where the friction component is around 40%. But the difference between the integrated forces and moments due to sideslip, as side force and yawing moment, in the two solutions are smaller than might be expected from the rather different flow patterns on the body presented above. The large discrepancies (of the order of 0-20%) found in the lateral coefficients between inviscid calculations and wind tunnel test results for the SÄNGER configuration in sideslip, that initiated this investigation, are not explained by the present results. It is however interesting to see that viscous and inviscid flow solutions that predict quite different flow topologies can give almost the same integrated aerodynamic forces, even though the surface pressure distribution differ locally. Also worth noticing is that the results from the approximative methods used to assemble the aerodynamic data set come very close to the results from the more complex methods used here.

Conclusions

Aerodynamic investigations performed on the SÄNGER vehicle in an early phase of the German Hypersonics Technology Programme revealed large discrepancies in the lateral coefficients between inviscid computations and wind tunnel results for sideslip cases. Viscous effects were suspected to be the origin of these discrepansies.

The purpose of the present investigation is to examine the influence of viscous effects on the aerodynamics of a hypersonic vehicle in sideslip. This is accomplished by computationally obtaining the flowfields governed by inviscid and viscous flow. The configuration chosen is the HYTEX R-A_3, and the flight case is defined by a Mach number of 3.5, an angle of attack of 2.01°, and a sideslip angle of -5.0° at 17.5 km altitude. Two computational grids are generated, one for the inviscid case containing approx. 1.05 million points, and one for the viscous case containing roughly 2.30 million points. In the viscous calculation the flow over the vehicle is assumed to be fully turbulent with a Reynolds number of 9.5 millions per meter. A two-equation turbulence model of κ-ε type is used to obtain the turbulent contribution to the flow.

The two flowfields exhibit both similarities and differences. At the front part of the vehicle the flowfields are very similar, up to the point where the main wings start. Further downstream, the viscous flow reveals a much more complex pattern with separated regions and vortices. The surface pressure distributions from the two solutions along the vehicle show a similar behavior. Upstream of the wings no difference is seen, but downstream where the flow topologies are different, a difference in the pressure is also observed. This is however not the case when comparing the integrated forces and moments on the vehicle. Very small differences are seen, except for a somewhat larger difference in yawing moment and a 40% increase in drag in the viscous solution due to the friction drag. The differences in the integrated forces and moments are not of the same order as found earlier between inviscid calculations and wind tunnel results for the SÄNGER vehicle. Various reasons could be seen why the present investigation differs from the SÄNGER results. The configurations are completely different and in the present Navier-Stokes computation the Reynolds number is much higher than in the wind tunnel test. For the moderate sideslip angle used in the present investigation, the flow around the long forebody of HYTEX is quite similar in the viscous and inviscid cases. It can therefore be assumed that larger differences will be seen between viscous and inviscid solutions for higher angles of attack and sideslip when vortices are formed along the nose in the viscous flowfield.

Acknowledgement

Major parts of the computational grids are generated by Petter Eneroth, FFA, Sweden. His effort in assembling the block topology and generating the computational grids is greatly appreciated.

This project was funded through a contract between the Swedish Space Corporation and Saab Ericsson Space within the framework of the German Hypersonic Technology Programme.

References

1. Blottner F. G., Verification of a Navier-Stokes Code for Solving the Hypersonic Blunt Body Problem, Proc Fourth Symposium on Numerical and Physical Aspects of Aerodynamic Flows, Jan. 1989.
2. Cucinelli G., HYTEX R-A_3 Aerodynamic Data Set Release 1.0, DASA Report LME12-HYPAC-TN-0386, July 1994.
3. Davidsson L., Implementation of a Semi-Implicit k-ε Turbulence Model into an Explicit Runge-Kutta Navier-Stokes Code, CERFACS, Rept. TR/RF/90/25, Toulouse, France, 1990.
4. Hirschel E., Arlinger B., Lind I., Nørstrud H., German -Scandinavian Cooperation in the Field of Aerothermodynamics of the German Hypersonics Technology Programme, AIAA Paper 95-6073, 1995.
5. Hirschel E., The Hypersonics Technology Development and Verification Strategy of the German Hypersonics Technology Programme, AIAA paper 93-5072, 1993.
6. Jameson A., Schmidt W., Turkel E., Numerical solutions of the Euler Equations by Finite Volume Methods using Runge-Kutta Time-Stepping Schemes, AIAA paper 81-1259, 1981.
7. Launder B. E., Sharma B. I., Application of the Energy Dissipation Model of Turbulence to the Calculation of Flows near a Spinning Disc, Letters in Heat and Mass Transfer, Vol. 1, 1974, pp. 131-138.
8. Sarkar S., Erlebacher G., Hussaini M., Kreiss H. O., The Analysis and Modelling of Dilatational Terms in Compressible Turbulence, ICASE Report No. 89-79, Dec. 1989.
9. Sillén M., Flow Simulation Around the Exact Canopy Geometry of the Spaceplane HERMES, AIAA Paper 93-5025, 1993.
10. Weingartner S., SÄNGER - The Reference Concept of the German Hypersonics Technology Program, AIAA Paper 93-5161, 1993.

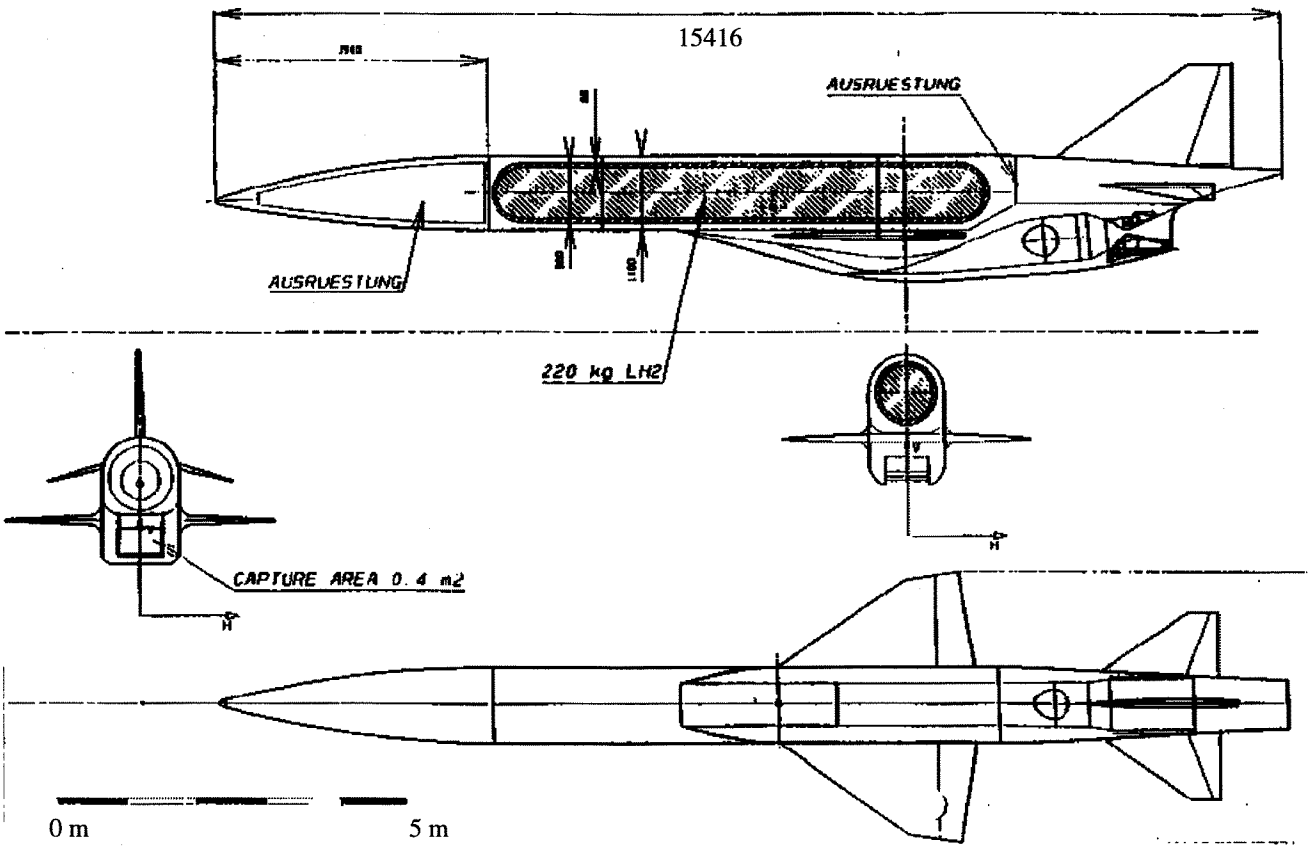

Figure 1 HYTEX R-A_3 layout.

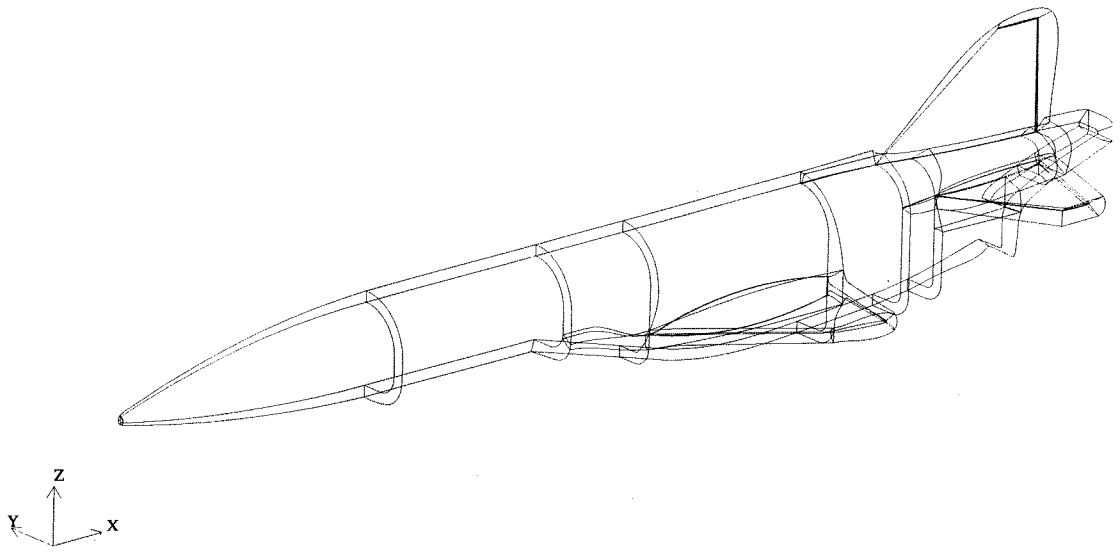

Figure 2 Near surface block structure in viscous grid.

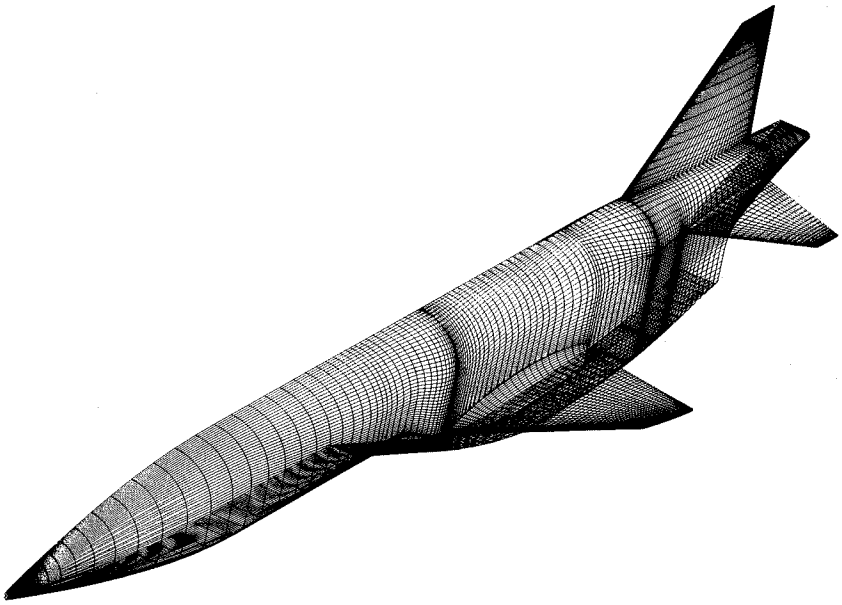

Figure 3 Surface grid.

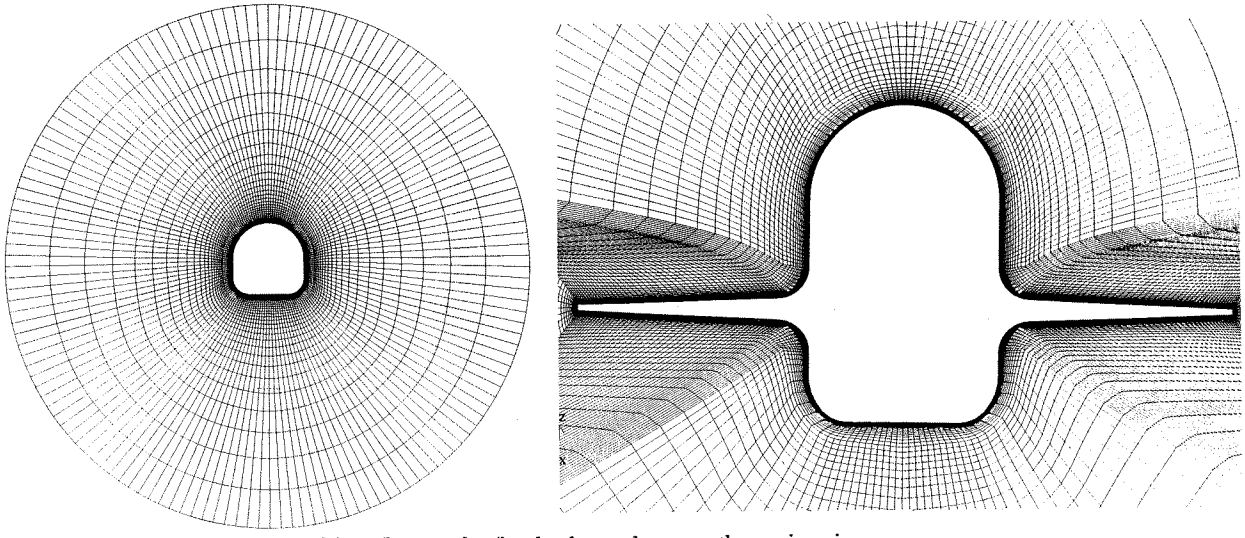

Figure 4 Cross plane grid surface at the forebody, and across the main wings.

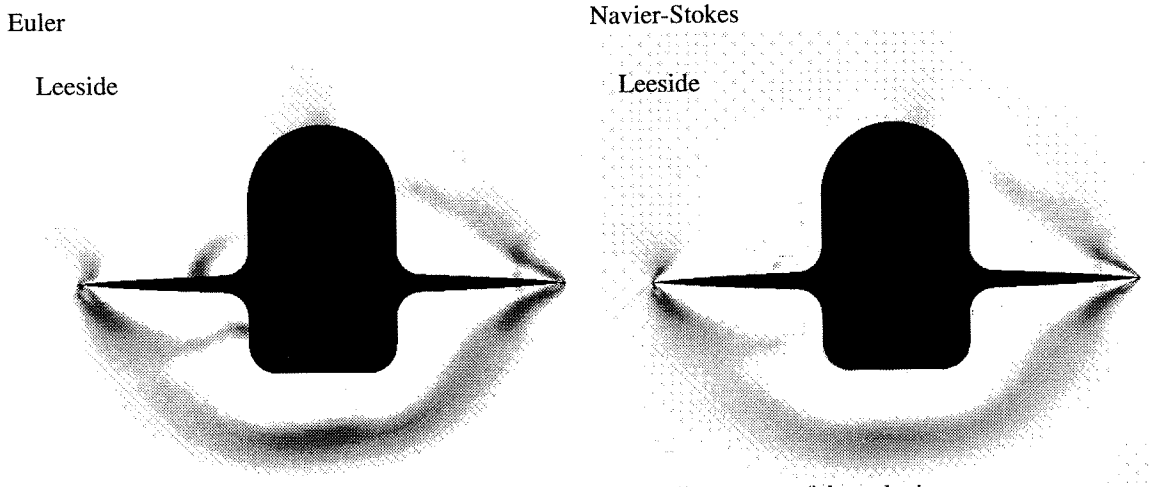

Figure 5 Shock wave pattern at x=10.0 m, visualized as the divergence of the velocity.

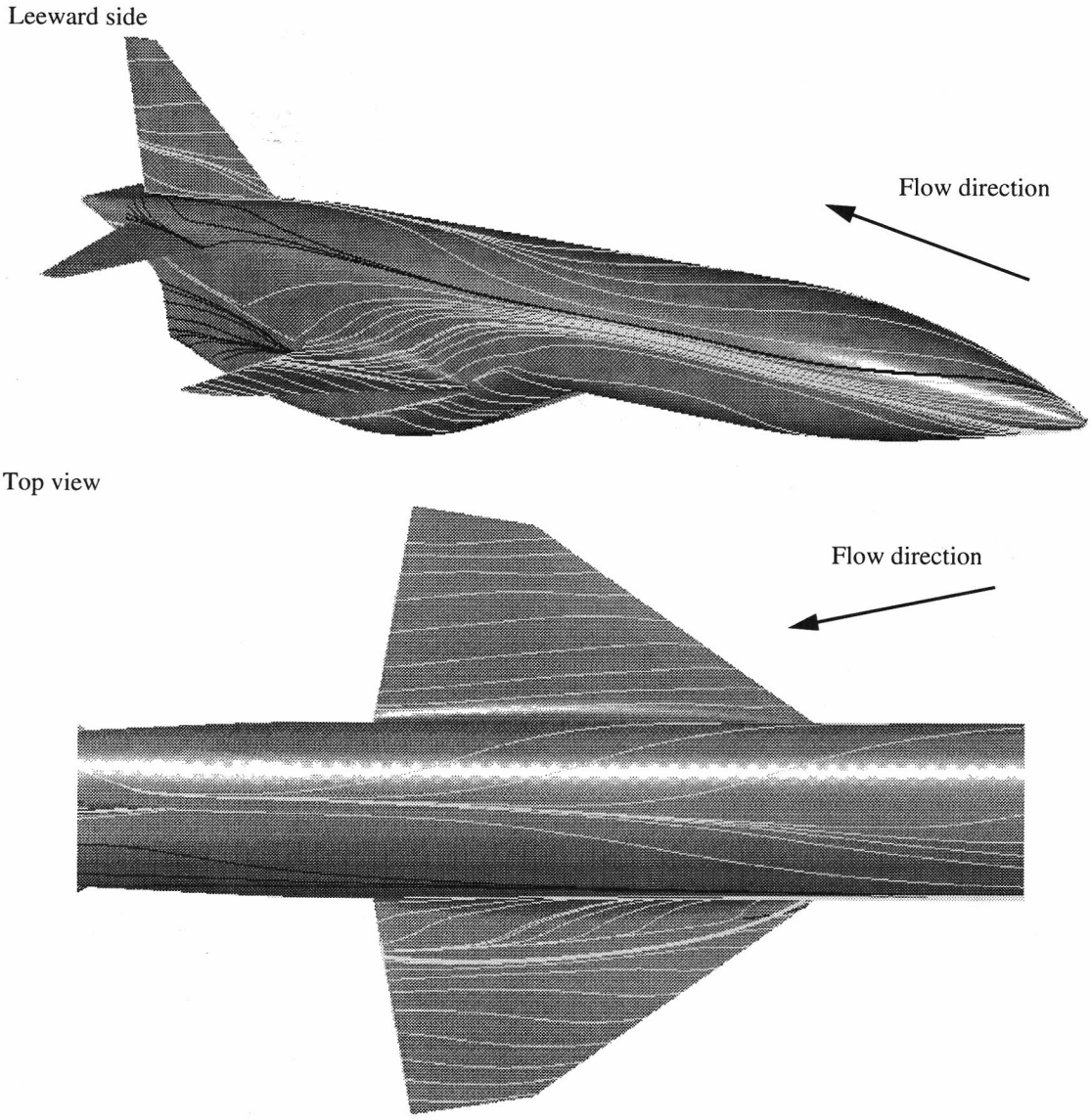

Figure 6 Skin friction lines in the viscous solution to reveal separation lines(bright) and reattachment lines(dark).

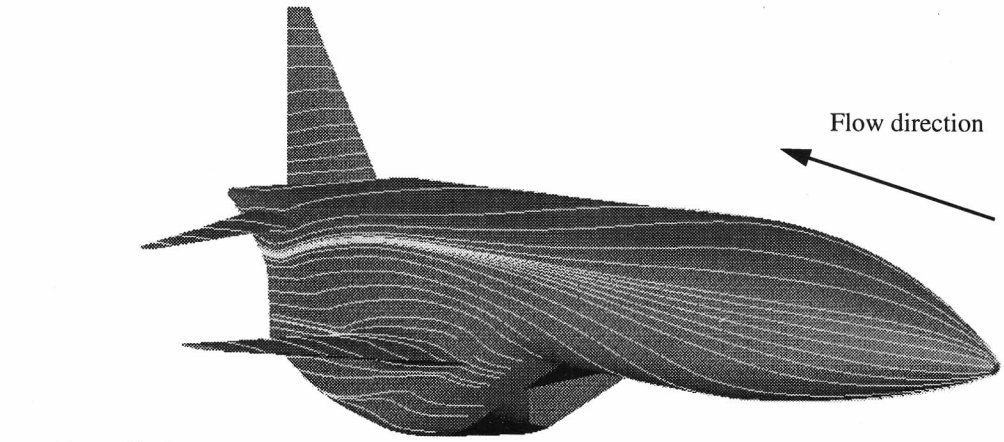

Figure 7 Surface streamlines in Euler solution

Leeward side

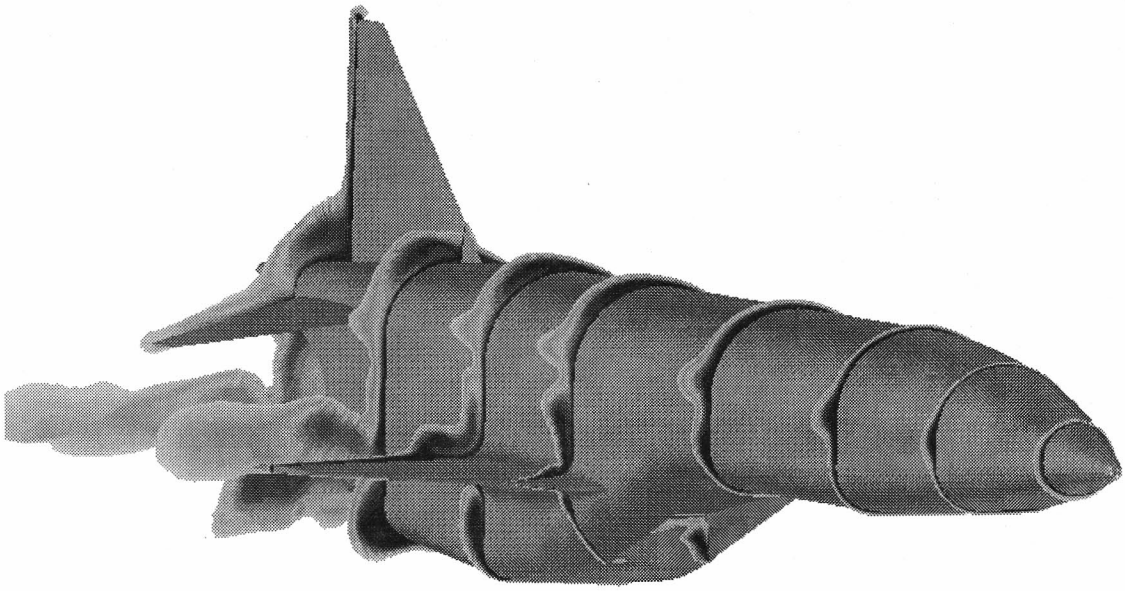

Figure 8 Total pressure distribution at some x-stations along the vehicle in the viscous solution.

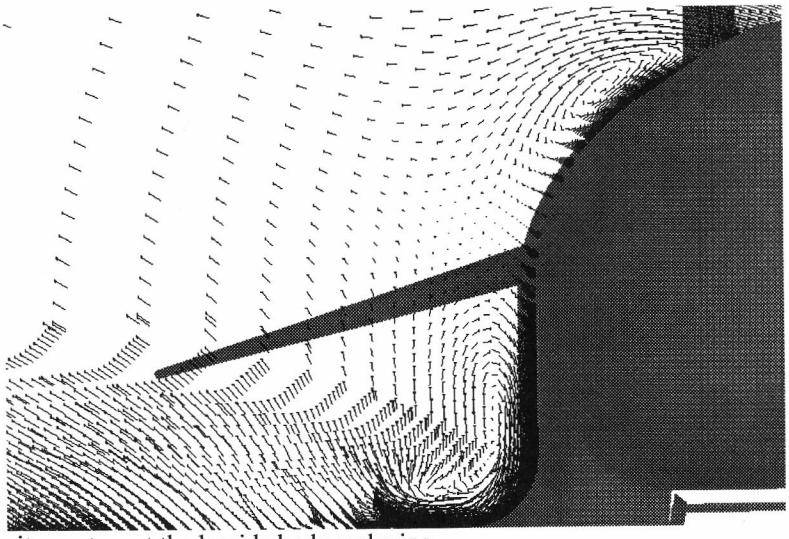

Figure 9 Velocity vectors at the leeside body and wing.

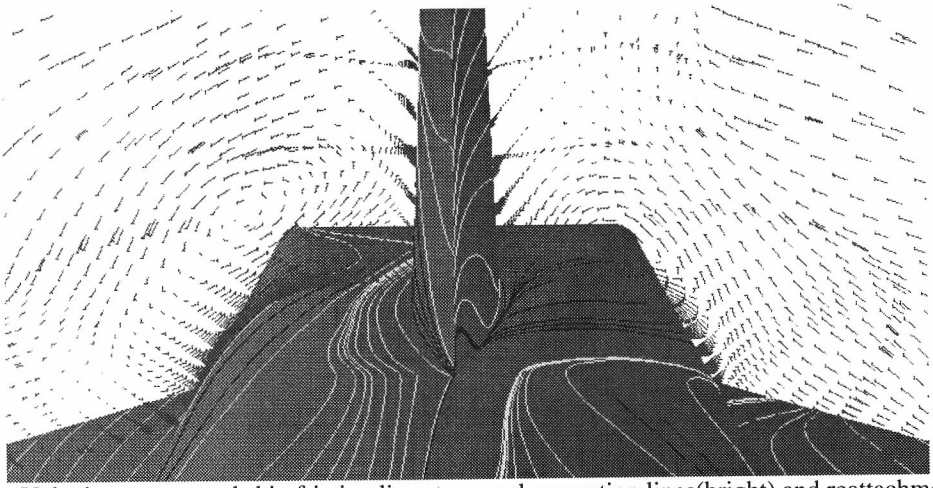

Figure 10 Velocity vectors and skin friction lines to reveal separation lines(bright) and reattachment lines(dark) at the tail, x=14.0 m.

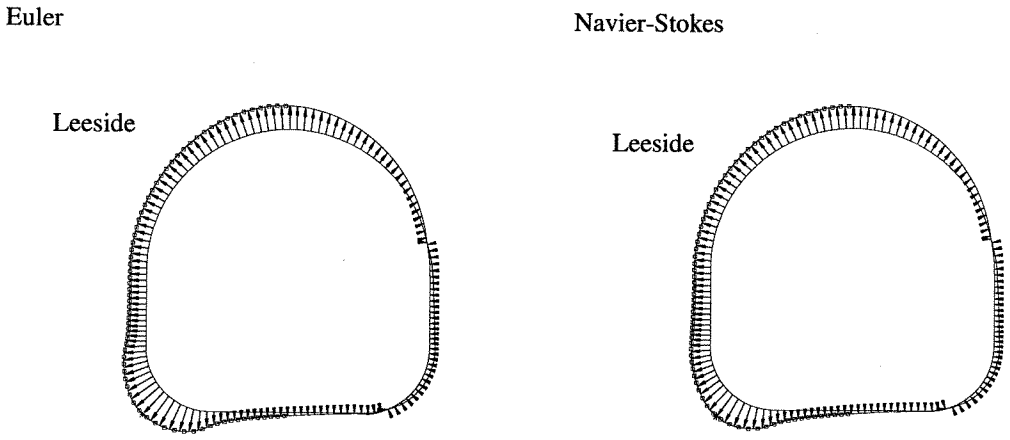

Figure 11 Pressure distribution at x=5.0 m.

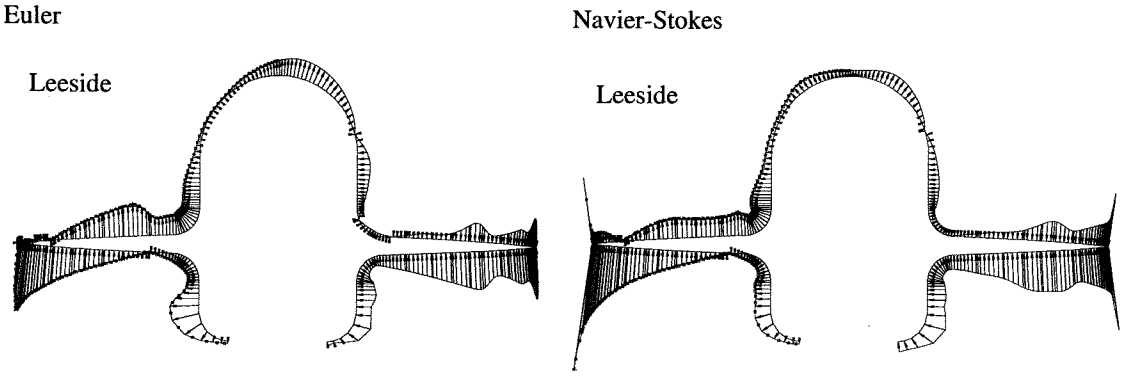

Figure 12 Pressure distribution at x=10.0 m.

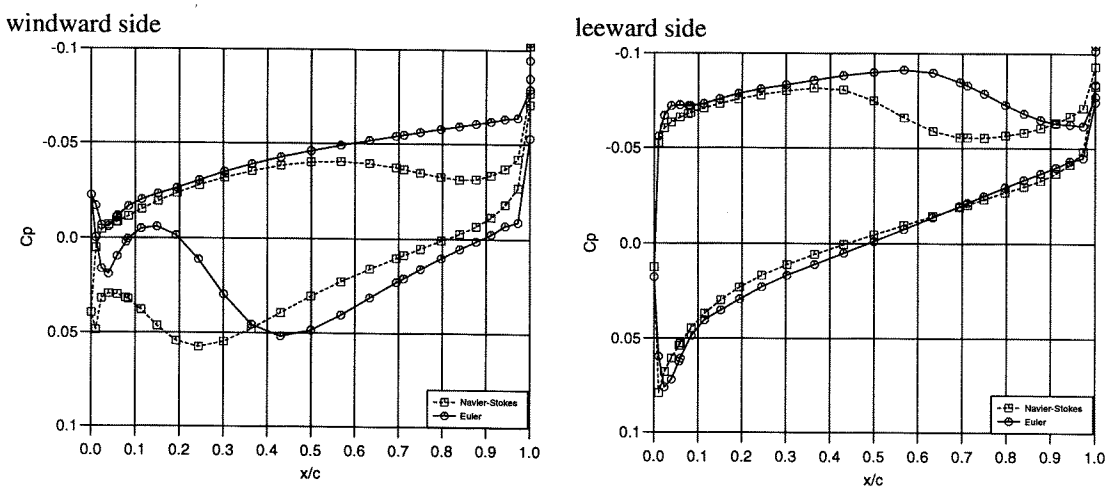

Figure 13 Chordwise pressure distribution on main wing, y=0.6 m, windward and leeward side.